GIS Odyssey Journal

2026 • Volume 6 • Number 1

https://doi.org/10.57599/gisoj.2026.6.1.121

Manoj Sarmah[1], Kesavan Dharanirajan[2], Nilakshi Mazumdar[3], Vishnu Manoj[4]

CLOUD-FREE FLOOD INUNDATION FREQUENCY MAPPING OF MAJULI ISLAND, ASSAM USING GOOGLE EARTH ENGINE AND SENTINEL-1 SAR TIME-SERIES (2017-2025)

Abstract: Majuli Island, located within the braided channel of the Brahmaputra in upper Assam, India and one of the most flood-prone landmasses in South Asia. Cloud-free flood inundation frequency mapping for Majuli Island exercise using dual Sentinel-1 SAR Ground Range Detected (GRD) workflows executed within Google Earth Engine. The results show that roughly 43.51% of the island was flooded at least once during the observation period. The annual flooded area ranged from 70 sq. km to 294 sq. km, with 2019 recording the largest extent. Validation against Sentinel-2 MNDWI reference imagery yielded a mean overall accuracy of 63.44% and a mean Kappa coefficient of 0.27. The mean spatial overlap with JRC Global Surface Water seasonal zones reached 88.57%. Over 61% of the island's agricultural land fell within the occasional-to-persistent flood frequency categories. The flood frequency dataset is intended as a direct operational input to embankment prioritisation, early warning planning, and agricultural risk assessment in Majuli.

Keywords: Majuli Island, Sentinel-1 SAR, flood frequency mapping, Google Earth Engine, Flood Frequency Index

Received: 6 May 2026; accepted: 22 May 2026; revised: 25 May 2026

[1] Pondicherry University, Department of Coastal Disaster Management, Research Scholar, Sri Vijaya Puram, Andaman & Nicobar Island, India, ORCID ID: https://orcid.org/0009-0009-5799-6594, email: manojsarmah1502@gmail.com

[2] Pondicherry University, Department of Coastal Disaster Management, Professor, Sri Vijaya Puram, Andaman & Nicobar Island, India, ORCID ID: https://orcid.org/0000-0003-1750-9893, email: dharanirajan@gmail.com

[3] Pondicherry University, Department of Coastal Disaster Management, Research Scholar, Sri Vijaya Puram, Andaman & Nicobar Island, India, ORCID ID: https://orcid.org/0009-0007-6562-0912, email: nilakshimazumdar22@gmail.com

[4] Pondicherry University, Department of Coastal Disaster Management, Research Scholar, Sri Vijaya Puram, Andaman & Nicobar Island, India, ORCID ID: https://orcid.org/0009-0002-5414-6243, email: vishnumanoj007@gmail.com

Introduction

Flooding kills more people and displaces more households than any other natural hazard class on earth. The UNDRR, 2022 estimates that the global toll between 2000 and 2019 was over 1.65 billion people affected and losses exceeding USD 651 billion. Within Asia, that burden falls disproportionately on the great monsoon-fed river systems, and none of them generates flood exposure as concentrated or as chronic as the Brahmaputra. The river drains about 580,000 sq. km across China, Bhutan, India and Bangladesh and it has one of the world's largest sediment loads. The Brahmaputra River monsoon peak discharge at the entry to the Assam plains is consistently greater than 60,000 cubic metres per second (Das, 2014; Goswami, 1985; Sarma, 2005). The result is a floodplain that not only floods in a bad year. It floods annually, as far back as records have gone.

The Majuli Island is located in the mid-channel of the Brahmaputra River between the main Brahmaputra to the north and the Kherkutia Xuti distributary to the south. It is the world's largest inhabited river island, although the island's total area has been shrinking at a rate that makes this distinction more and more hollow. In 1891, the island's area was roughly 1,256 sq. km, but by 2013 it had reduced to 522 sq. km. The island lost 58% due to the combined effects of bank erosion and flooding (Borah et al., 2018; DDMA Plan Majuli 2022-2023; Sarma, 2005). Beyond that, the island is culturally significant and is home to the Vaishnavite satras, monastic institutions founded by Srimanta Sankardeva in the 15th and 16th centuries. Whose mask traditions, manuscripts and performing arts have influenced the culture of the Brahmaputra valley for centuries (Sahariah et al., 2013).

Each year, the Brahmaputra floods and inundates croplands, villages and wetlands. Every year, a few hundred families are evacuated and in bad years thousands (Chetia, 2013; Deka et al., 2024). Such as the 2019 monsoon, which was bad enough to trigger emergency notices from the Assam State Disaster Management Authority (DDMA Plan Majuli 2022-2023.; Saikia et al., 2024). But despite this level of recurrent loss, the spatial pattern of flood recurrence, i.e. where on the island flooding occurs, and in how many of the previous decades, has never been documented at a level of detail that would be helpful to an engineer planning where to construct embankments, or a planner designing evacuation routes. There is quite a bit of research on riverbank erosion on Majuli (A. K. Das et al., 2012; Kotoky et al., 2005), but not on flood frequency.

The South Asian monsoon blankets northeastern India in cloud from June through October. During precisely the months when flooding is worst, satellite-based optical sensors, such as Landsat, Sentinel-2, and IRS, are largely useless for flood detection because they cannot penetrate clouds. Studies in Assam and elsewhere in the region report peak monsoon cloud cover of 80-90% (Singha et al., 2020; Uddin et al., 2019). This is not an edge case; it is the norm, and it explains why optical remote sensing studies of floods in this region tend to use before-and-after imagery from the margins of the monsoon rather than images taken during actual inundation.

SAR sensors work in the microwave spectrum and are unaffected by cloud cover or rainfall. They detect surface water through the sharp drop in backscattered signal that occurs when a rough or vegetated land surface is replaced by a smooth water surface, which reflects radar energy away from the sensor rather than scattering it back (Mason et al., 2012; Schumann & Moller, 2015). The ESA Sentinel-1 mission has made this approach accessible at scale. Sentinel-1A launched in April 2014; Sentinel-1B joined it in 2016, establishing six-day repeat coverage over most continental land areas at 10-metre spatial resolution in Interferometric Wide swath mode (Torres et al., 2012). The archive now spans more than a decade of monsoon seasons.

Google Earth Engine hosts petabytes of satellite data server-side, and runs distributed geospatial computation without requiring local downloads or high-performance hardware (Gorelick et al., 2017). Several groups have used GEE-Sentinel-1 combinations to map monsoon floods in Bangladesh and India with results that hold up reasonably well against optical validation data where cloud-free conditions permit comparison (Singha et al., 2020; Twele et al., 2016; Uddin et al., 2019). None of those studies, as far as we can establish, has applied this approach across a full decade specifically to build a pixel-level flood frequency map for a Brahmaputra floodplain island. That is the gap this paper fills.

Four objectives structure the work. First, to extract annual monsoon-season inundation extents for Majuli across 2017 to 2025 using bi-temporal VH backscatter change detection. Second, to generate a pixel-level Flood Frequency Index from ten years of VV-polarisation annual flood masks covering 2017 to 2025. Third, to quantify flood exposure at the Panchayat and land-use class level against the FFI output. Fourth, to validate SAR-derived flood extents against Sentinel-2 MNDWI reference data and JRC Global Surface Water seasonal zones. The intended audience is not only the remote sensing research community but also the planners, engineers, and disaster managers working on the Brahmaputra floodplain who need spatially grounded, multi-year flood recurrence data to make defensible investment decisions.

Materials and methods

Study area and data source. Majuli lies in upper Assam, between 26°45′N to 27°12′N (latitude) and 93°39′E to 94°35′E (longitude) (Figure 1). Since 2016, it has been constituted as a separate administrative district under the Government of Assam, reportedly the first river island to achieve district status in India. The island is almost perfectly flat; elevations range between roughly 80 and 90 metres above mean sea level, and the soils are unconsolidated alluvium that erodes rapidly under both fluvial and wave action. The island receives an average rainfall between 1,800 and 2,200 mm per year from June to October.

The southwestern section of the island is the weakest because of the confluence of the Subansiri River with the Brahmaputra. It increases discharge and sediment load in an overburdened channel system, where embankment breaches have often occurred in the last 30 years (CWC, 2019; Kotoky et al., 2005). The island is extensively cultivated

for paddy rice under different cropping patterns, such as ahu (summer rice), bao (deep-water rice), and sali (winter rice), and is punctuated by wetland depressions (locally known as beels), riparian and semi-evergreen forest stands, grasslands, and the nucleated villages around the satras.

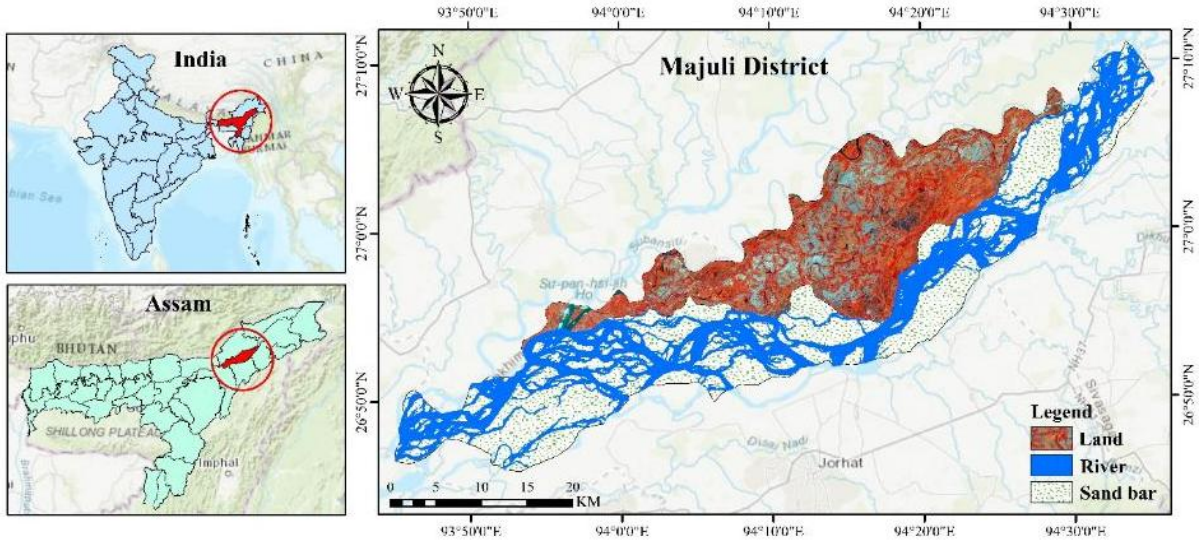

Figure 1. Study area map

Source: Prepared by the author; administrative boundaries from the Survey of India

Satellite data were acquired and processed using GEE (Gorelick et al., 2017), removing the need for local storage or download chains and allowing the processing to be repeated without special equipment (Table 1).

Table 1. Datasets used in the study

Dataset	Source	Spatial Resolution	Temporal Coverage	Purpose
Sentinel-1 GRD (IW, VV, VH)	ESA / GEE	10 m	2017-2025 (monsoon seasons)	Flood inundation extraction
SRTM DEM	USGS / GEE	30 m	Static	Slope masking; terrain analysis
JRC Global Surface Water v1.4	JRC / GEE	30 m	1984-2021	Permanent water masking; spatial validation
Sentinel-2 MSI L2A	ESA / GEE	10 m	Four validation seasons	Optical accuracy validation via MNDWI
Majuli administrative boundary	District GIS	Vector	Current	Area-of-interest definition
Panchayat boundaries	District GIS	Vector	2011	Zonal exposure statistics

Source: Compiled by the author from ESA, USGS, JRC, and District GIS

The main data source was Sentinel-1 GRD images in Interferometric Wide (IW) swath mode, containing the VV and VH polarisation bands. ESA's Level-1 GRD processing encompasses thermal noise removal, radiometric calibration and Range-

Doppler terrain correction; all of this is retained in the GEE archive (Torres et al., 2012). The SRTM DEM (Farr et al., 2007) was used to mask terrain-induced artefacts via the slope layer. JRC Global Surface Water v1.4 (Pekel et al., 2016) was used to mask permanent water bodies before flood mapping and provides a high-resolution spatial reference for validation, through its layer of seasonal water-occurrence. Sentinel-2 L2A Surface Reflectance imagery was applied for the optical accuracy assessment in four years where flood maps could be independently extracted based on cloud-free conditions.

Overview of the processing framework. The processing framework consists of SAR data acquisition and pre-processing in Google Earth Engine (GEE), followed by annual inundation mapping using bi-temporal backscatter change detection, the development of a multi-year Flood Frequency Index, and accuracy assessment through zonal exposure analysis. Two distinct Sentinel-1 processing pipelines were employed throughout the study, differing in polarisation, orbital direction, and analytical objectives. These pipelines are described separately to preserve the clarity of the methodological rationale, as combining them into a single workflow would obscure the underlying design considerations (Figure 2).

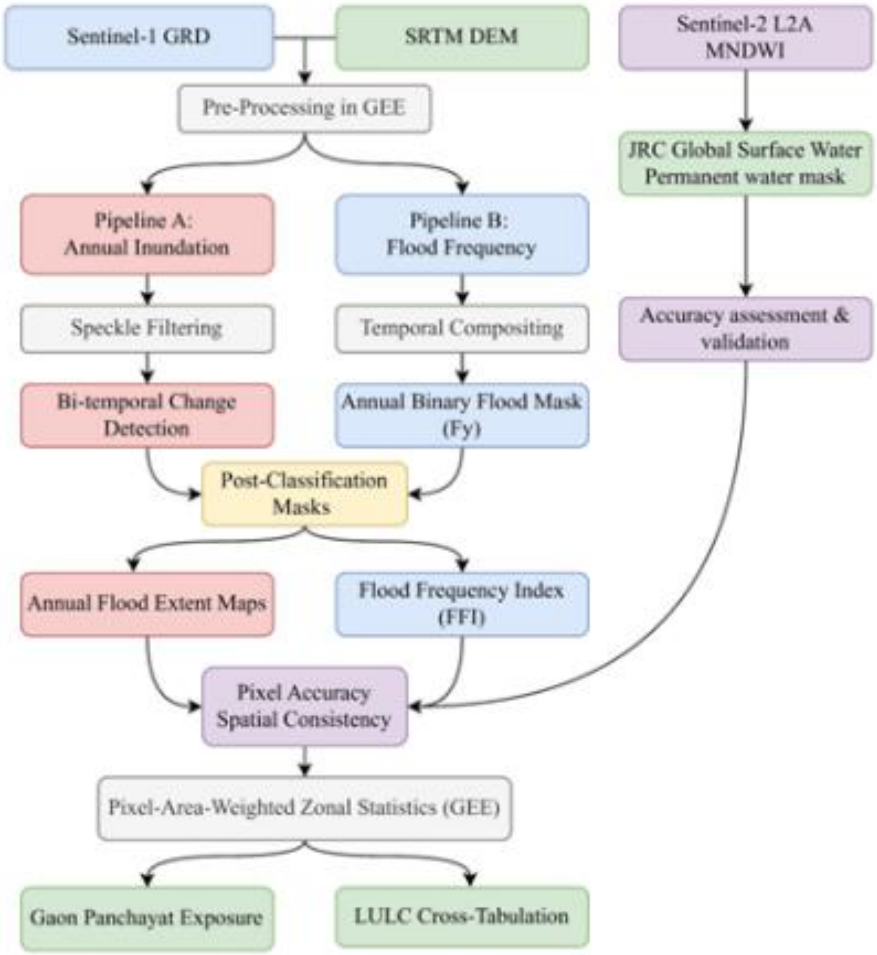

Figure 2. Methodology flow chart of the study
Source: Author's own elaboration

Pre-processing of Sentinel-1 data. Sentinel-1 operates in C-band at 5.4 GHz. In IW mode, it covers a 250 km swath at a nominal ground resolution of 10 m. ESA's standard GRD processing chain handles thermal noise removal, radiometric calibration, and terrain correction before archiving, so those steps do not need to be replicated (Torres et al., 2012). In the GEE platform orbit filtering, speckle suppression, and temporal compositing are applied.

The annual inundation pipeline filtered images to the Majuli boundary, the IW mode, VH polarisation availability, and descending orbit passes only. Fixing the orbit direction is not a minor point. Ascending and descending acquisitions observe the same surface from different angles, and mixing them across seasons introduces incidence-angle-driven backscatter variation that can look like land-cover change even when nothing on the ground has changed (Twele et al., 2016). Using descending passes consistently ensures that year-to-year backscatter differences actually reflect surface change rather than viewing geometry. VH cross-polarization was chosen because paddy fields and vegetated land in general scatter energy more strongly in the cross-polarized channel, making the backscatter drop that occurs when flooding begins easier to detect against the background noise floor (Martinis et al., 2015).

Speckle filtering was applied per image before compositing: a focal mean filter with a one-pixel circular kernel run over two iterations. This suppresses the salt-and-pepper noise that would otherwise produce isolated false flood detections at individual pixels. The flood frequency pipeline took a different approach: no per-image filtering was applied, and instead the median reducer used during compositing served as the primary noise control step. The median is a natural outlier suppressor in a multi-scene stack and performs that role without the spatial smoothing that comes with a filter kernel (Twele et al., 2016).

Flood inundation extraction. Annual flood inundation was extracted for each monsoon season from 2017 to 2025 using a bi-temporal SAR backscatter change detection approach. For each year y, two temporal windows were defined. Pre-flood reference period starts from 1 April - 31 May of year y (dry/pre-monsoon season) and flood-peak period starts from 1 June - 31 October of year y (peak monsoon season). Flood detection was based on the physical principle that inundated surfaces exhibit significantly lower SAR backscatter compared to non-flooded vegetation or bare soil, as smooth open water causes specular reflection of radar energy away from the sensor. The backscatter difference between the pre-flood baseline and flood-peak composites was computed as:

$$\Delta\sigma_y^0 = \sigma_{\text{pre}}^0 - \sigma_{\text{flood}}^0 \qquad \text{eq. 1}$$

where values are expressed in decibels (dB). Pixels where $\Delta\sigma_y^0 \geq T$(threshold T) were classified as flooded in year y. A threshold value of T = 3 dB was adopted following established practices in SAR-based flood mapping studies, which have demonstrated that a backscatter decrease of ≥ 3 dB reliably distinguishes temporary floodwater from background land surfaces (Du et al., 2026; Martinis et al., 2015). The threshold was

further refined through visual inspection of flood extents against Sentinel-2 optical imagery for selected cloud-free flood events.

Three post-classification masks were applied sequentially to minimise commission errors. Permanent water mask classified pixels as permanent water bodies (JRC Global Surface Water occurrence ≥ 90%) were excluded to isolate temporary flood inundation from perennial water bodies such as rivers and beels. Slope mask pixels on terrain slopes exceeding 5° (derived from the SRTM DEM) were excluded to eliminate false detections caused by SAR layover and shadow effects on sloping surfaces. Minimum-area filter isolated flooded patches smaller than 0.1 ha (approximately 10 pixels at 10 m resolution) were removed to suppress salt-and-pepper noise in the classification output. The result for each year y is a binary flood mask $F_y(x)$, defined as:

$$F_y(x) = \begin{cases} 1 & \text{if pixel } x \text{ is flooded in year } y \\ 0 & \text{otherwise} \end{cases} \quad \text{eq. 2}$$

The annual inundated area (sq. km) was quantified by multiplying each flooded pixel by its geodesic area using GEE's ee.Image.pixelArea() function, followed by a region-wide summation at a 10 m spatial scale. The inundated area was subsequently expressed as a %age of the total island area (522.73 sq. km) and assigned an ordinal flood severity class (Table 2).

Table 2. Annual flood inundation severity classification

Inundation %age (%)	Severity Class
< 25	Low
25 - 35	Moderate
35 - 45	High
45 - 55	Very High
> 55	Extreme

Source: Compiled by the author based on the inundation percentage analysis

Flood Frequency Mapping. Annual binary flood masks for all nine years (2017-2025) were stacked into a multi-temporal image collection within GEE. A pixel-level Flood Frequency Index (FFI) was computed by summing all annual binary flood masks across the study period:

$$FFI(x) = \sum_{y=2017}^{2025} F_y(x) \quad \text{eq. 3}$$

where $FFI(x) = 0$, indicates a pixel never inundated during 2017-2025, and $FFI(x) = 9$ indicates a pixel flooded across all nine monsoon seasons. The continuous FFI raster was reclassified into five flood frequency categories based on natural breaks and domain knowledge (Table 3).

The flood frequency map and class-wise area statistics (sq. km) were computed using a grouped region reduction (ee.Reducer.sum().group()) at 30 m spatial scale and exported in GeoTIFF format at 10 m resolution in UTM Zone 46N (EPSG:32646), appropriate for the geographic location of Assam.

Table 3. Flood frequency classification scheme (2017-2025)

Class	FFI Range (years)	Category	Description
0	0	Never Flooded	No inundation detected during 2017-2025
1	1-2	Rare	Inundated in 1-2 out of 9 years
2	3-5	Occasional	Inundated in 3-5 out of 9 years
3	6-7	Frequent	Inundated in 6-7 out of 9 years
4	8-9	Persistent	Inundated in 8-9 out of 9 years

Source: Compiled by the author based on flood frequency analysis (2017–2025)

Accuracy assessment and validation. The accuracy of the SAR-derived annual flood inundation maps was evaluated through a two-tier validation framework: (i) quantitative pixel-level accuracy assessment against Sentinel-2 MSI optical reference data, and (ii) spatial consistency verification against the JRC Global Surface Water dataset.

For the quantitative accuracy assessment, Sentinel-2 Level-2A (Surface Reflectance) imagery was used as an independent reference for validation. Validation years (2019, 2020, 2022, and 2023) were selected on the basis of cloud-free scene availability (cloud cover < 20%) during the monsoon flood peak period (June-October). Cloud and cloud shadow pixels were masked using the Sentinel-2 Scene Classification Layer (SCL), and a median composite was generated from all qualifying acquisitions within the flood window for each validation year. Flood extent from Sentinel-2 was delineated using the Modified Normalised Difference Water Index (MNDWI), computed as:

$$MNDWI = \frac{\rho_{Green} - \rho_{SWIR1}}{\rho_{Green} + \rho_{SWIR1}} \quad \text{eq. 4}$$

where ρ_Green and ρ_SWIR1 correspond to Sentinel-2 Bands B3 and B11, respectively. Pixels with MNDWI > 0 were classified as flooded, following the exclusion of permanent water bodies (JRC occurrence ≥ 90%) and steep terrain (slope > 5°). The Sentinel-2 MNDWI-derived flood extent served as the reference (actual) layer, against which the SAR-derived flood mask (predicted) was evaluated. A stratified random sampling approach was adopted, with 200 sample points per class (flooded and non-flooded), ensuring balanced representation of both classes and avoiding bias in accuracy estimation due to class imbalance. A pixel-level error (confusion) matrix was constructed from the sampled points, from which the following accuracy metrics were derived: Overall Accuracy (OA), Kappa Coefficient (κ), Producer's Accuracy (PA), and User's Accuracy (UA) (Congalton, 1991).

For the spatial consistency verification, the SAR-derived flood masks were overlaid with the JRC seasonally inundated zones, defined as pixels with historical water occurrence between 10% and 90% in the JRC Global Surface Water v1.4 dataset (Pekel et al., 2016).These zones represent areas with documented episodic inundation history and serve as a spatially independent benchmark for verifying whether the SAR-detected flood extents are geographically consistent with established inundation patterns.

The spatial consistency index was computed as the %age of SAR-detected flood area that spatially overlaps with JRC seasonal water zones:

$$JRC\ Consistency\ (\%)\ = \frac{Area_{SAR \cap JRC_seasonal}}{Area_{SAR_flood}} \times 100 \qquad \text{eq. 5}$$

Zonal statistics. An identical pixel-area-weighted zonal statistics procedure was independently applied to quantify the spatial distribution of flood exposure across administrative and land cover units. For each spatial framework, the analytical workflow commenced with the construction of a dual-band composite raster. In the geodesic pixel area was derived from the native ee.Image.pixelArea() function and rescaled to square kilometres was stacked alongside the classified flood frequency raster encoding inundation recurrence across five ordinal classes over the nine-year observation period from 2017 to 2025. This composite image was overlaid on each respective vector layer using the reduceRegions() operation. It performs a spatially explicit grouped summation via ee.Reducer.sum().group(), which partitioned cumulative pixel area within each polygon simultaneously by flood class membership. Both analyses were conducted at a spatial resolution of 30 metres under the Universal Transverse Mercator Zone 46N coordinate reference system (EPSG:32646), with a tile scale factor of 16 applied uniformly to accommodate the computational memory demands of fine-resolution. The nested dictionary output for each polygon was subsequently pivoted on the server into a normalised, flat tabular structure using an iterative routine, assigning each flood class index to a descriptively labelled attribute column and defaulting to zero for absent classes. The resulting feature collections provide one record per Gaon Panchayat unit and one per LULC polygon. Each contains five area columns spanning the full flood frequency class spectrum, enabling parallel quantitative comparisons of flood exposure at both the administrative and land-cover levels of analysis.

Results

Sentinel-1 data coverage. Processing across both pipelines consumed a total of 187 Sentinel-1 GRD scenes. Coverage for 2015 and 2016 was sparser, reflecting the single-satellite phase before Sentinel-1B joined the constellation and established six-day revisit capability over Assam (Torres et al., 2012). From 2017 onward, consistent descending-orbit acquisitions were available for every monsoon season. The fixed descending orbit constraint in the annual inundation pipeline held the sensor incidence angle stable across all nine study years, which is necessary to make inter-annual backscatter comparisons meaningful.

Annual Flood Extents (2017-2025). The bi-temporal VH change-detection approach delineated inundation extents across all nine monsoon seasons. Flood inundation map of Majuli Island (2025) showing the spatial distribution of flood-affected areas in red, with Garamur marked as the district headquarters. (**Błąd! Nie można odnaleźć źródła odwołania.**, Figure 4). The year-to-year variation is large. The 2019 season produced roughly 294 sq. km of detected inundation, 56.33% of the total island area, classified as

Extreme Table 4. This matches documented reports from the Assam State Disaster Management Authority and the Central Water Commission, both of which recorded multiple embankment breaches in Majuli that season and the displacement of over 5,000 families (ASDMA, 2019; CWC, 2019). At the other end, only about 70 sq. km were flooded in 2021. The IMD characterised the 2021 northeast India monsoon as significantly below normal in rainfall totals, which is consistent with this result (IMD, 2021).

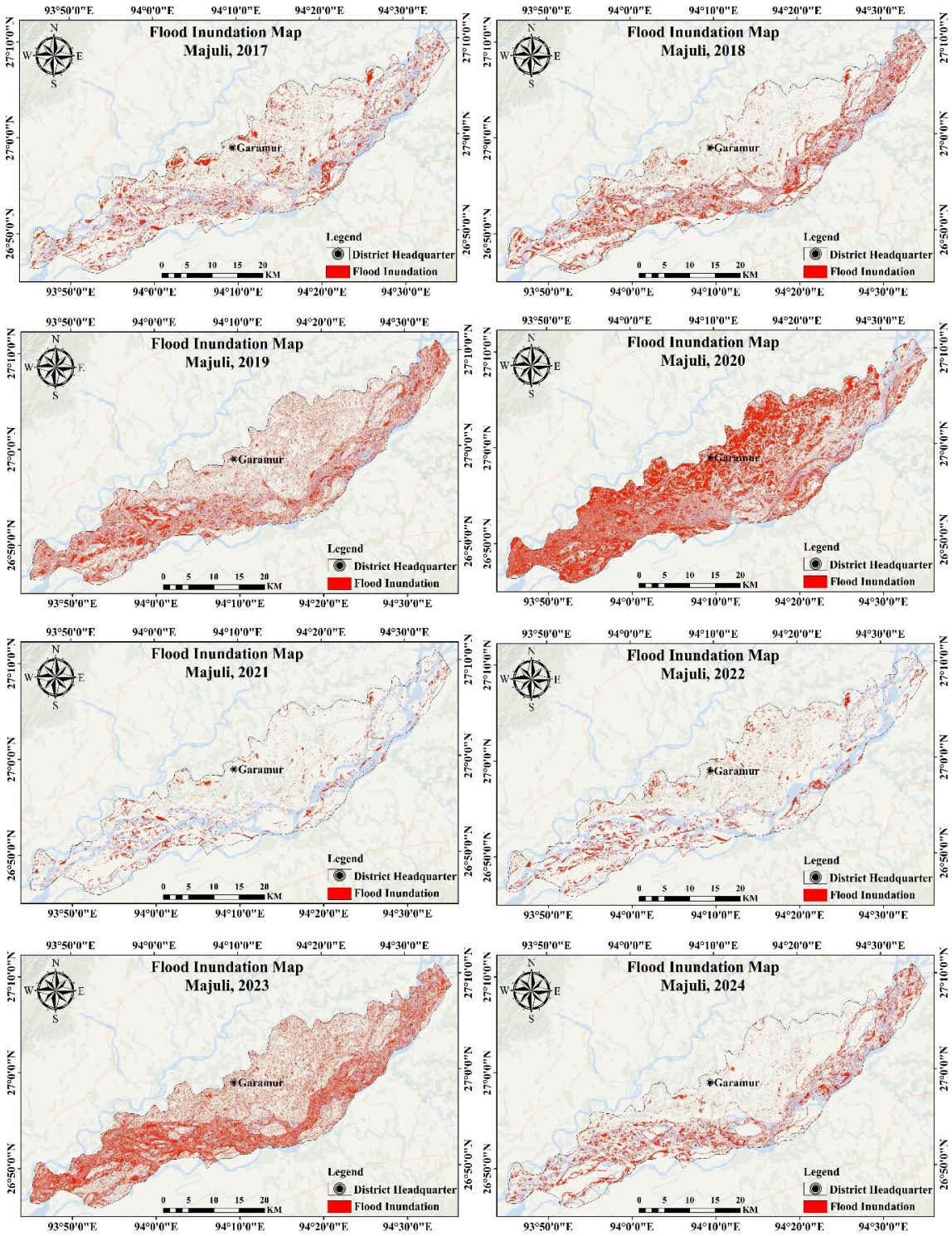

Figure 3. Flood inundation map of Majuli from 2017 to 2022
Source: Prepared by the author using Google Earth Engine and ArcGIS

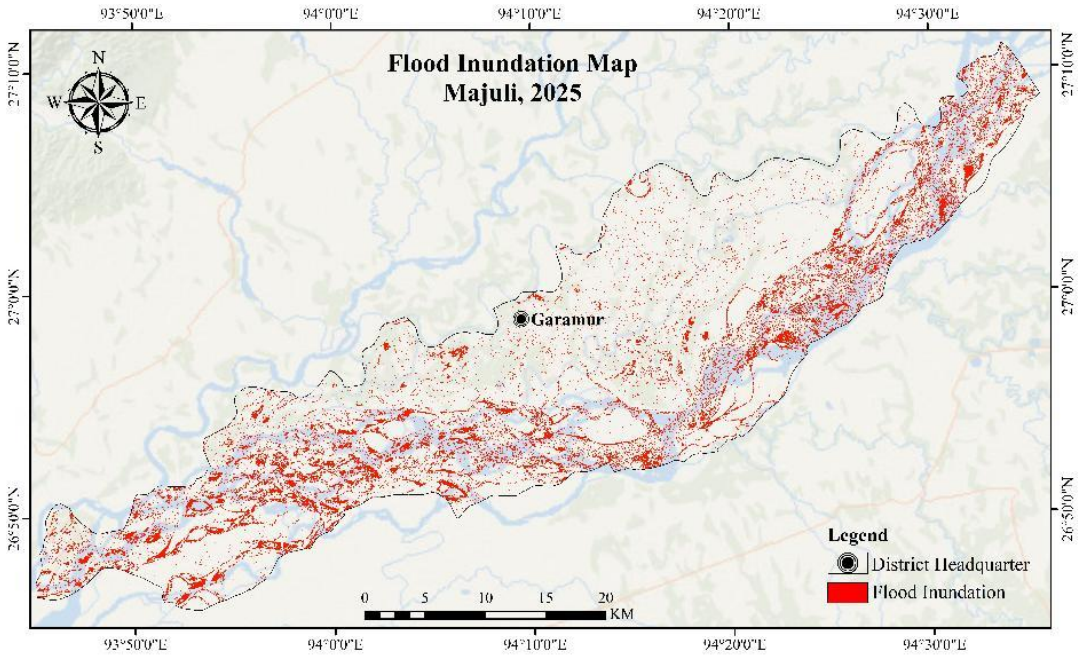

Figure 4. Flood inundation map of Majuli, 2025
Source: Prepared by the author using Google Earth Engine and ArcGIS

Spatially, the pattern is consistent across high-flood years. Inundation concentrates in the southwestern and central sectors. The eastern fringe and the modestly elevated ridges around the larger satra settlements remain largely unaffected, even in extreme years. It is no coincidence that the settled areas occupy the highest available micro-terrain on the island, a land-use pattern that almost certainly reflects long historical experience of flood risk.

Table 4. Annual flood inundation area and severity class, Majuli Island (2017-2025)

Year	Inundated Area (sq. km)	%age of Island Area	Flood Severity
2017	195.24	37.4	High
2018	244.15	46.77	Very High
2019	294.02	56.33	Extreme
2020	181.93	34.84	Moderate
2021	70.37	13.48	Low
2022	100.76	19.3	Low
2023	203.5	38.99	High
2024	180.11	34.5	Moderate
2025	186.91	35.81	High

Source: Author's own classification and area calculation

Flood frequency index distribution. The decade-long VV pipeline produced a highly variable spatial map of FFI at the pixel scale (Figure 5). The FFI ranges from 0 to 10, with 0 indicating no inundation and 10 indicating inundation in every season.

43.51% of the island was inundated at least once during the decade. FFI 9 to 10, covers an area of about 15.14 sq. km and is highly focused along the southern channel margin and in the deep wetland depressions (

Table 5). The frequent flood terrain, FFI 6 to 8 adds another 6.03 sq. km and predominantly runs along the margins of embankment-enclosed regions where overtopping is an annual event.

Table 5. Area by flood frequency class, Majuli Island (2017-2025)

Class	Category	FFI Range	Area	
			sq. km	%age
0	Never Flooded	0	266.90	56.49
1	Rare	1-2	244.69	14.97
2	Occasional	3-5	470.91	22.31
3	Frequent	6-8	158.63	6.03
4	Persistent	9-10	15.41	0.21

Source: Author's own classification and area calculation

There is a distinct northwest-southeast gradient in the pattern. The highest FFI values are along the southern bank, where the Brahmaputra channel has been shifting southwards in recent decades (Borah et al., 2018; Kotoky et al., 2005). As the channel approaches, the width of the river-embankment gap decreases, the chance of embankment overtopping increases, and the FFI captures that as the pixel values rise. Embankments in the north seem to have done a decent job of keeping flood waters out, and their FFI values are largely in the rare and occasional classes. The FFI of the core settlement areas of Garamur, Kamalabari, and Auniati ranges from 1 to 3, as would be expected for flood refuges for the surrounding population.

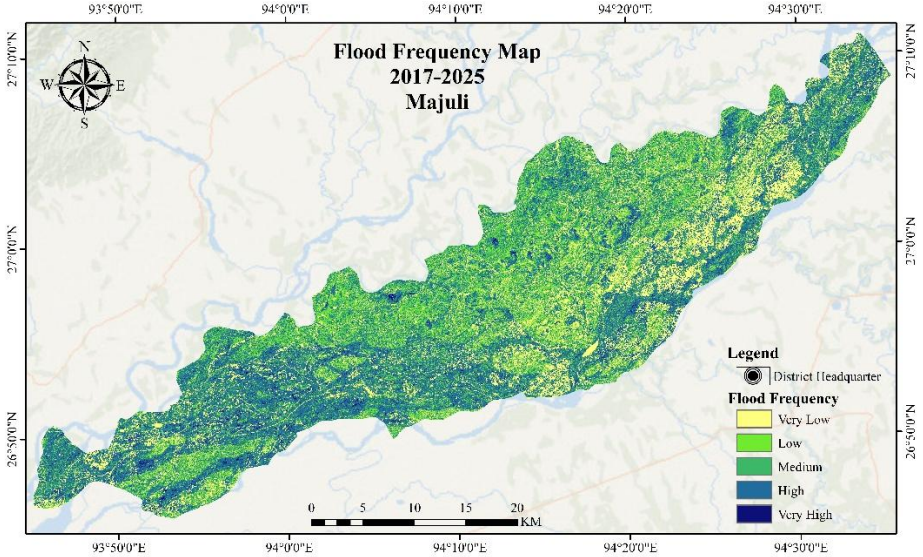

Figure 5. Flood Frequency Map, Majuli

Source: Prepared by the author using Google Earth Engine and ArcGIS

Validation. The overall accuracy for the four validation years varied between 54% (2022) and 69% (2023) with an average of 63.44%. The Kappa coefficient ranged from 0.08 to 0.38. Based on the Landis & Koch, 1977 standards, this suggests fair to moderate agreement (Table 6). The largest flood area detected by SAR occurred in 2023 and had the highest accuracy. This is reasonable; a large contiguous flood extent has fewer mixed pixels along the flood's perimeter, compared to the flood's extent, which leads to fewer errors at the perimeter (Singha et al., 2020).

The 2022 results warrant particular scrutiny, as the Kappa coefficient of 0.08 approximates random agreement. This performance can be attributed to three primary factors. First, extensive cloud cover during the 2022 flood peak necessitated construction of the reference Sentinel-2 composite from multi-day acquisitions across the flood window, rather than a single near-peak scene, thereby introducing temporal mismatch. Second, as a low-to-moderate flood year on Majuli, 2022 featured substantial partial inundation, resulting in a high proportion of mixed pixels along flood margins where both sensors captured transitional flood conditions. Third, there is a compositional difference between SAR composites, which use all acquisitions in the June-October window, and optical composites, which can only use the subset of cloud-free acquisitions in that window. This temporal misalignment is a well-known and documented weakness of cross-sensor validations of flooding in tropical monsoon regions, not a problem in the SAR approach itself (Chini et al., 2019; Twele et al., 2016).

The JRC spatial consistency results are more stable. Across the four years, an average of 88.57 % of the flood pixels identified by SAR were found within the JRC seasonal water zone. The 99.04 % in 2019 is the highest value and, in a sense, indicates that the extent of the SAR-detected flood in that extreme flood year was completely within the extent that JRC's 35-year record had already identified as seasonally inundated. The 2022 figure of 74.79 % is the lowest, coinciding with other 2022 anomalies.

Table 6. Accuracy assessment results for SAR-derived flood maps

Year	OA (%)	Kappa	SAR Flood Area (km2)	JRC Overlap (km2)	JRC Consistency (%)
2019	66.75	0.335	15.39	15.25	99.04
2020	64	0.28	58.84	52.24	88.77
2022	54	0.08	24.63	18.42	74.79
2023	69	0.38	76.08	69.76	91.69
Mean	63.44	0.269	43.74	38.92	88.57

Source: Author's own analysis

Panchayat-Level Flood Exposure. Spatial zonal analysis of mean FFI values for Majuli's panchayats found a high degree of variation in values across the administrative zones. The most noticeable panchayats with mean FFI values of 7 to 9 (frequent-to-persistent) were south-western Dakhin Ahotguri, Karatipar and Ahotguri. Garamur and adjacent central panchayats on elevated terrain had mean values of 1.5-2.8 (Table 7).

The five most vulnerable panchayats accounted for 38% of the island's total persistently inundated area. A concentration that suggests that chronic flood risk is not uniformly spread, but is highly concentrated, with direct consequences for resource planning (Figure 6).

The communities most heavily affected are predominantly Mishing, an indigenous group with long-established practices of flood adaptation including elevated stilt-house construction and post-flood paddy farming. Those adaptations provide genuine protection in moderate flood years but become inadequate when embankments breach entirely and inundation is both deep and prolonged.

Table 7: Panchayat-level flood frequency class distribution

Block	Panchayat	Area In %				
		Never (0)	Rare (1-2)	Occasional (3-5)	Frequent (6-8)	Persistent (9-10)
Majuli	Ahotguri	18.12	14.29	44.10	21.03	2.46
	Bongaon	35.26	22.74	33.10	8.30	0.60
	Chilakola	13.80	32.55	43.44	8.68	1.53
	Dakhin Ahotguri	14.43	13.30	45.77	23.72	2.78
	Dakhin Kamalabari	17.99	21.25	45.03	14.48	1.25
	Dakhin Pat	32.46	21.30	33.99	11.11	1.14
	Garamur	18.70	32.00	43.39	5.75	0.15
	Kamalabari	21.46	30.18	39.90	7.81	0.66
	Karatipar	14.21	20.79	46.02	17.37	1.61
	Pokajora	16.45	33.78	41.13	7.64	1.00
	Rawnapar Chamaguri	36.02	30.76	28.74	4.21	0.27
	Sri Luit	15.22	30.69	42.31	10.73	1.05
Ujani Majuli	Cherpai	24.41	29.82	39.64	5.92	0.20
	Jengrai	14.30	28.06	46.42	10.40	0.83
	Luit Poria	35.25	24.10	32.85	7.30	0.50
	Phuloni	16.01	33.69	42.77	7.05	0.48
	Rangachahi	24.94	31.39	35.75	7.10	0.83
	Ratanpur Miri	26.81	19.04	40.37	12.80	0.98
	Ratanpur Gayan	29.08	20.50	35.53	13.32	1.57
	Sriram	25.19	28.14	38.45	7.64	0.57

Source: Author's own analysis

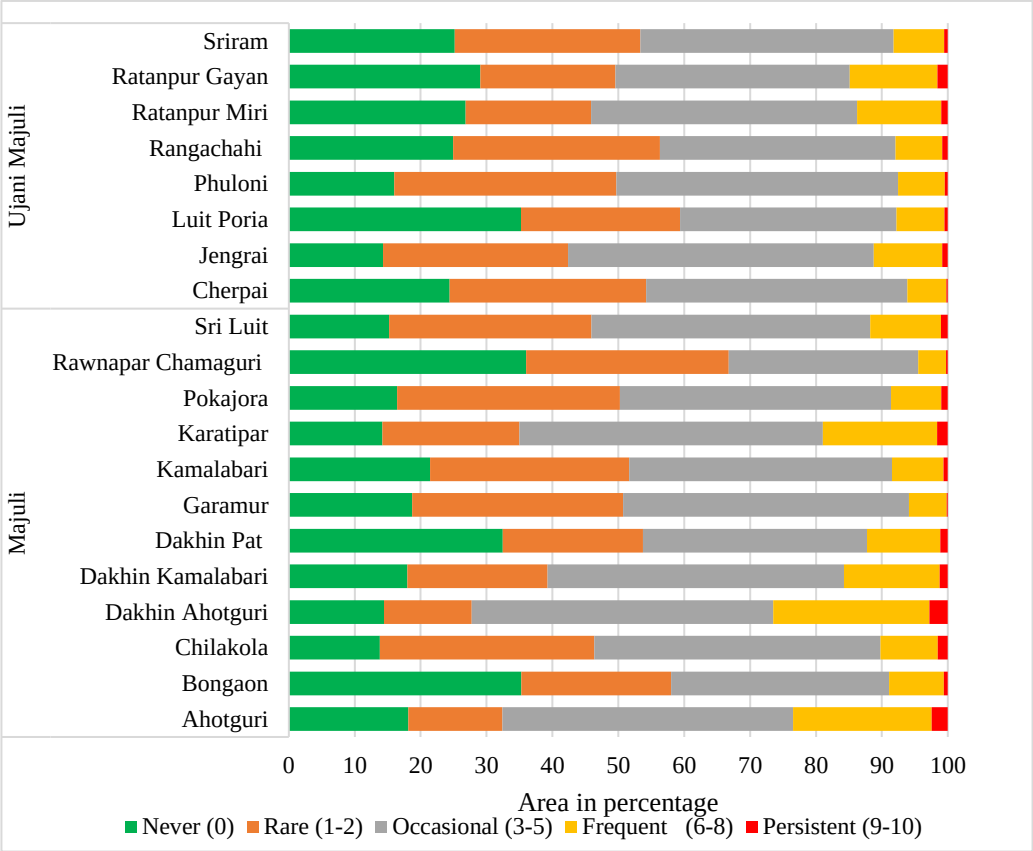

Figure 6. Spatial distribution of flood frequency categories across Majuli
Source: Author's own analysis

LULC Cross-Tabulation. Agricultural land carries the largest absolute flood exposure of any LULC class on the island. Approximately 61.4 % of all agricultural pixels fell within the occasional-to-persistent FFI range (Table 8). Wetlands dominated the persistent flood class, accounting for 78.3 % of all persistent pixels, which is expected, since the beel wetlands by definition occupy the lowest-lying depressions and hold water longest after inundation events. Settlement pixels concentrated in the rare and occasional categories, reflecting the historically elevated micro-terrain on which permanent settlements were established (Figure 7).

Table 8. LULC class distribution across flood frequency categories

LULC Class	Area In %				
	Never (0)	Rare (1-2)	Occasional (3-5)	Frequent (6-8)	Persistent (9-10)
Rivers & Waterbodies	24.86	14.29	41.51	17.53	1.82
Char Lands	23.99	16.02	41.44	16.88	1.68
Natural Vegetation	34.66	26.81	33.59	4.79	0.15
Settlement Area	31.34	30.86	34.06	3.68	0.07
Agricultural Land	18.24	32.55	40.78	7.79	0.65

Source: Author's own analysis

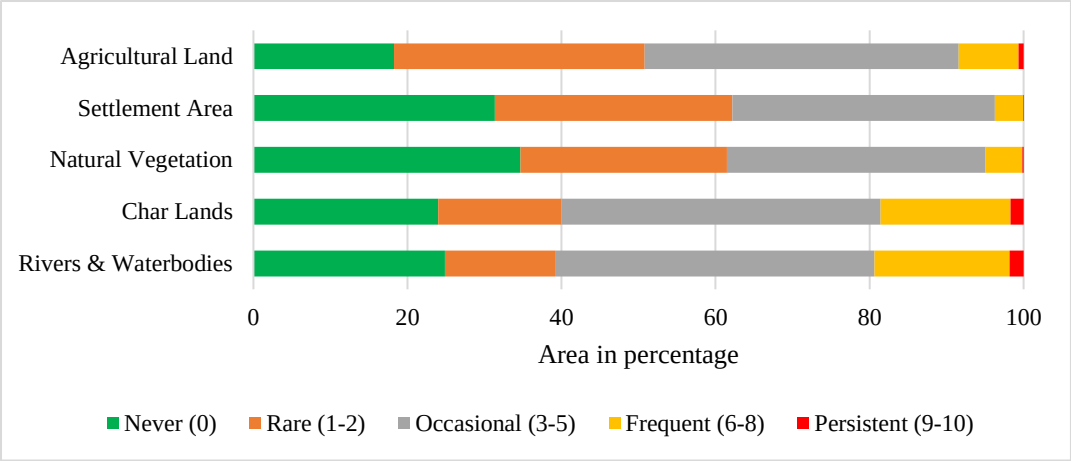

Figure 7. Flood frequency distribution pattern across land-use and land-cover classes in Majuli
Source: Author's own analysis

Discussion

There have been many studies of the loss of landmass in Majuli over time (A. K. Das et al., 2012; Kotoky et al., 2005; Sarma, 2005). These studies answer the question of where the island is shrinking. The FFI map answers where, within the remaining land area, flooding occurs, and how often. It's not the same question, and it's not the same answer. A parcel of land that erodes away is lost; a parcel of land that floods nine years out of ten, but is still present in the next dry season, poses a cyclical damage problem that has consequences for the people who live and work on it, but is not detected by area change.

The other related existing work are flood-susceptibility models. Majuli and other AHP susceptibility maps for places along the Brahmaputra floodplain essentially assign pixels a score based on their slope, soil type, proximity to channels, and other static variables (Das et al., 2012). These are valuable models but they predict potential likelihood, not past events. A pixel with a high AHP flood susceptibility may or may not flood in any given decade, depending on the strength of the monsoon, water releases upstream, and the integrity of embankments. The FFI represents history, not potential, and that makes it useful for designing insurance, prioritising embankment investments and planning land-use in ways that susceptibility scores are not.

Agricultural risk and food security. The finding that 61.4% of Majuli's farmland is in the occasional-to-persistent flood-frequency category is more than a number. It is the business model for rice cultivation. Ahu rice, which is cultivated in March and harvested before the peak of the monsoon, is the flood-tolerant variety of the three main rice crops grown on Majuli; bao, the traditional deep-water rice, is adapted to withstand extended periods of inundation. The winter rice, sali, which makes the greatest contribution to household food security and market income, is planted after the recession of the monsoon and is susceptible to late inundation and sediment loading, which affects soil health. The Mishing and Deori villages in the high-FFI southwestern panchayats suffer

the cumulative impact of crop losses, planting delays and soil degradation due to sediment accretion.

The point in this is the specificity. The FFI doesn't tell us Majuli is a flood-prone island; we know that. It says what 29 sq. km are flooded in almost every year, what 31 sq. km flood in 6 to 8 of 10 years, and which panchayats have the most of this area. Crop insurance products in Assam have until now been offered at district or larger scales; sub-panchayat FFI data at 10-metre resolution would permit parametric insurance products to be priced and offered at the resolution where farmers are located.

SAR Framework Performance. The dual-polarisation pipeline design was deliberate, and the results justify it. VH backscatter in paddy-dominant terrain captures the transition from wet, volume-scattering canopy to flooded canopy cover that characterises early monsoon inundation before complete submergence (Singha et al., 2020). That sensitivity makes VH suited to annual inundation extraction, where the goal is to detect the maximum seasonal extent, including shallow and partial flooding. VV backscatter produces a stronger specular return from smooth, open water surfaces and provides more consistent detection across the range of flood depths and durations encountered in a ten-year stack. Using VV for the frequency pipeline and VH for the annual extraction yields different information from the same sensor, in a way a single-polarisation approach cannot replicate.

The overall accuracy figures of 54-69% and Kappa values of 0.08-0.38 are not numbers to be proud of in isolation. In context, they fall within the range routinely reported for SAR-based monsoon flood mapping across South and Southeast Asia, where optical validation data are structurally compromised by the same cloud cover that motivates the SAR approach. Singha et al., (2020) Working in Bangladesh has obtained OA of 62-71% and Kappa of 0.24-0.35, and Uddin et al., (2019), working in similar conditions, reported comparable ranges. The 88.57% mean JRC spatial consistency is arguably the more reliable performance indicator because it does not depend on cloud-free optical acquisitions and reflects spatial correspondence with an independent 35-year water-occurrence archive.

Limitations. The 3 dB fixed threshold will generate some commission errors in densely vegetated areas where double-bounce scattering between standing stems and flooded ground partially compensates for the surface-smoothing backscatter drop. Adaptive Otsu thresholding, as described by (Martinis et al., 2015), could reduce this problem but adds complexity to the processing chain. The 6-12-day revisit cycle means that flash flood events shorter than the revisit interval will not be captured. Validation for 2022, 2023, and 2024 relied exclusively on Sentinel-2 optical data, which in those years was cloud-affected enough to compromise validation quality. This is a data availability problem, not a methodological one, and it will be resolved as the JRC product is updated.

Conclusion

This study produced the first pixel-level flood-inundation frequency map for Majuli Island, derived from a complete multi-year SAR time series. Using two complementary Sentinel-1 processing pipelines within Google Earth Engine, we mapped annual monsoon-season inundation extents across 2017 to 2025 and constructed a Flood Frequency Index from ten years of VV-polarisation flood masks covering 2017 to 2025. The all-weather SAR approach bypassed the optical cloud cover barrier that has historically prevented direct flood monitoring in northeastern India during monsoon conditions. Almost three-quarters of the island experienced flooding at some time. The persistent flood terrain is found along the southwestern margin of the channel where the ongoing southward movement of the Brahmaputra is eroding the boundary between the river and land. The annual flooded area ranged from 70 to 294 sq. km, depending on the strength of the monsoon, with 2019 being a stand-out extreme year in line with reported embankment breaches and population displacement. Over 61% of the island's croplands were in the occasional to persistent flood frequency class, a statistic that has direct consequences for crop yield and livelihood of the Mishing and Deori farmers who own that land.

The mean accuracy of 63.44% and mean Kappa of 0.27 are moderate, while the 2022 season results are near random agreement with the optical reference. The more reliable mean JRC spatial consistency of 88.57% is similar to other studies in South Asia. The approach is completely replicable and can be updated in near real time as Sentinel-1 acquisitions become available in the GEE archive, so that it can be used as a tool rather than just a research product. The immediate applications include prioritisation of embankments in flood-prone regions, design of a panchayat-level flood early warning system, design of parametric agricultural insurance boundaries, and land-use planning when habitable surface is declining. Future analysis incorporating flood depth from hydrodynamic modelling, ascending and descending orbit passes for improved temporal resolution, and socioeconomic vulnerability data would be a holistic flood risk assessment for the island.

Funding

This research received no specific grant from any funding agency in the public, commercial, or not-for-profit sectors.

Declaration of Competing Interests

The authors declare that they have no known competing financial interests or personal relationships that could have appeared to influence the work reported in this paper.

Data Availability

The data used in this study were obtained from the Google Earth Engine Data Catalog, a publicly accessible archive of satellite imagery and geospatial datasets. The specific

datasets and their identifiers are provided in the Methods section. Any processed outputs generated during the current study are available from the corresponding author upon reasonable request.

Use of Generative AI and AI-Assisted Technologies

No generative AI or AI-assisted technologies were employed in the preparation of this manuscript.

References

ASDMA (2019). Assam flood, 2019. Assam State Disaster Management Authority, Government of Assam. https://asdma.assam.gov.in/sites/default/files/swf_utility_folder/departments/asdma_revenue_uneecopscloud_com_oid_70/menu/document/assam_flood_memorandum_2019.pdf.

Borah S. B., Sivasankar T., Ramya M.N.S., Raju P.L.N. (2018). Flood inundation mapping and monitoring in Kaziranga National Park, Assam using Sentinel-1 SAR data. Environmental Monitoring and Assessment, 190(9), 520. https://doi.org/10.1007/s10661-018-6893-y.

Chetia M. (2013). Disasters-Induced Displacement vis-à-vis Policy Framework: A Study of the Mishing Community of Majuli, Assam. Disaster & Development, 7. https://doi.org/https://nidm.gov.in/journal/PDF/Journal/2_Dec_2013/2_Dec_2013d.pdf.

Chini M., Pelich R., Pulvirenti L., Pierdicca N., Hostache R., Matgen P. (2019). Sentinel-1 InSAR Coherence to Detect Floodwater in Urban Areas: Houston and Hurricane Harvey as A Test Case. Remote Sensing, 11(2), 107. https://doi.org/10.3390/rs11020107.

CWC (2019). ANNUAL REPORT CENTRAL WATER COMMISSION Department of Water Resources, River Development & Ganga Rejuvenation, Ministry of Jal Shakti 2019-2020. https://www.cwc.gov.in/sites/default/files/arcwc2019-20.pdf.

Das A.K., Sah R.K., Hazarika N. (2012). Bankline change and the facets of riverine hazards in the floodplain of Subansiri–Ranganadi Doab, Brahmaputra Valley, India. Natural Hazards, 64(2), 1015–1028. https://doi.org/10.1007/s11069-012-0283-5.

Das D. (2014). Majuli in Peril: Challenging the received wisdom on flood control in Brahmaputra River Basin, Assam (1940–2000). Water History, 6(2), 167–185. https://doi.org/10.1007/s12685-014-0098-2.

DDMA Plan Majuli 2022-2023. (n.d.). https://majuli.assam.gov.in/sites/default/files/public_utility/DDMA%20Plan_compressed.pdf.

Deka P., Chowdhury G., Saha A.K. (2024). Impact of Landuse and Landcover Changes on Population Dynamics in Flood-prone Majuli Island, Assam, India. Human Ecology, 52(3), 531–548. https://doi.org/10.1007/s10745-024-00504-6.

Du M., Shao Z., Xiao X., Zhang J., Zhu D., Wang J., Balz T., Li D. (2026). High-precision flood change detection with lightweight SAR transformer network and context-aware attention for enriched-diverse and complex flooding scenarios. ISPRS Journal of Photogrammetry and Remote Sensing, 231, 507–531. https://doi.org/10.1016/j.isprsjprs.2025.11.011.

Farr T.G., Rosen P.A., Caro E., Crippen R., Duren R., Hensley S., Kobrick M., Paller M., Rodriguez E., Roth L., Seal D., Shaffer S., Shimada J., Umland J., Werner M., Oskin M., Burbank D., Alsdorf D. (2007). The Shuttle Radar Topography Mission. Reviews of Geophysics, 45(2), 2005RG000183. https://doi.org/10.1029/2005RG000183.

Gorelick N., Hancher M., Dixon M., Ilyushchenko S., Thau D., Moore R. (2017). Google Earth Engine: Planetary-scale geospatial analysis for everyone. Remote Sensing of Environment, 202, 18–27. https://doi.org/10.1016/j.rse.2017.06.031.

Goswami D.C. (1985). Brahmaputra River, Assam, India: Physiography, Basin Denudation, and Channel Aggradation. Water Resources Research, 21(7), 959–978. https://doi.org/10.1029/WR021i007p00959.

IMD (2021). Report on Northeast Monsoon, 2021. https://mausam.imd.gov.in/chennai/mcdata/ne_monsoon_2021.pdf.

Kotoky P., Bezbaruah D., Baruah J., Sarma J.N. (2005). Nature of bank erosion along the Brahmaputra river channel, Assam, India. CURRENT SCIENCE, 88(4). https://www.jstor.org/stable/24110266.

Landis J.R., Koch G.G. (1977). The measurement of observer agreement for categorical data. Biometrics, 33(1), 159–174. https://doi.org/https://doi.org/10.2307/2529310.

Martinis S., Kersten J., Twele A. (2015). A fully automated TerraSAR-X based flood service. ISPRS Journal of Photogrammetry and Remote Sensing, 104, 203–212. https://doi.org/10.1016/j.isprsjprs.2014.07.014.

Mason D.C., Davenport I.J., Neal J.C., Schumann G.J.-P., & Bates P.D. (2012). Near Real-Time Flood Detection in Urban and Rural Areas Using High-Resolution Synthetic Aperture Radar Images. IEEE Transactions on Geoscience and Remote Sensing, 50(8), 3041–3052. https://doi.org/10.1109/TGRS.2011.2178030.

Pekel J.-F., Cottam A., Gorelick N., Belward A.S. (2016). High-resolution mapping of global surface water and its long-term changes. Nature, 540(7633), 418–422. https://doi.org/10.1038/nature20584.

Sahariah D., Singha K., Bora D.K., Kundu S., Das T., Sen S., Das K., Mili,B., Baruah, J., Sarma K., Saikia M., Saikia A. (2013). Majuli at the Crossroads: A Study of Cultural Geomorphology. Space and Culture, India, 1(2), 12–20. https://doi.org/10.20896/saci.v1i2.26.

Saikia T., Kakoti M., Hazarika J., Panika T.P., Bezbaruah A., Choudhury S.A., Goswami, P. (2024). Assessing Multi-Decadal Landmass Changes and River Bank Erosion in the Char Areas of Majuli River Island of Assam, India. Journal of Scientific Research and Reports, 30(8), 201–211. https://doi.org/10.9734/jsrr/2024/v30i82240.

Sarma J.N. (2005). Fluvial process and morphology of the Brahmaputra River in Assam, India. Geomorphology, 70(3–4), 226–256. https://doi.org/10.1016/j.geomorph.2005.02.007.

Schumann G.J.-P., Moller D.K. (2015). Microwave remote sensing of flood inundation. Physics and Chemistry of the Earth, Parts A/B/C, 83–84, 84–95. https://doi.org/10.1016/j.pce.2015.05.002.

Singha M., Dong J., Sarmah S., You,N., Zhou Y., Zhang G., Doughty R., Xiao X. (2020). Identifying floods and flood-affected paddy rice fields in Bangladesh based on Sentinel-1 imagery and Google Earth Engine. ISPRS Journal of Photogrammetry and Remote Sensing, 166, 278–293. https://doi.org/10.1016/j.isprsjprs.2020.06.011.

Torres R., Snoeij P., Geudtner D., Bibby D., Davidson M., Attema E., Potin P., Rommen B., Floury N., Brown M., Traver I.N., Deghaye P., Duesmann B., Rosich B., Miranda N., Bruno C., L'Abbate M., Croci R., Pietropaolo A., … Rostan F. (2012). GMES Sentinel-1 mission. Remote Sensing of Environment, 120, 9–24. https://doi.org/10.1016/j.rse.2011.05.028.

Twele A., Cao W., Plank S., Martinis, S. (2016). Sentinel-1-based flood mapping: A fully automated processing chain. International Journal of Remote Sensing, 37(13), 2990–3004. https://doi.org/10.1080/01431161.2016.1192304.

Uddin K., Matin M.A., Meyer F.J. (2019). Operational Flood Mapping Using Multi-Temporal Sentinel-1 SAR Images: A Case Study from Bangladesh. Remote Sensing, 11(13), 1581. https://doi.org/10.3390/rs11131581.

UNDRR (2022). Global Assessment Report on Disaster Risk Reduction 2022: Our World at Risk: Transforming Governance for a Resilient Future (1st ed). United Nations Publications. https://www.undrr.org/media/79595/download?startDownload=20260613.